

## Controllable optical-sideband generation and synchronization in a mechanical gain-loss optomechanical system

Souvik Mondal<sup>1,\*</sup> and Kapil Debnath<sup>1,2,†</sup>

<sup>1</sup>*Electronics and Electrical Communication Engineering Department, IIT Kharagpur, West Bengal 721302, India*

<sup>2</sup>*School of Natural and Computing Sciences, University of Aberdeen, Aberdeen AB24 3UE, United Kingdom*



(Received 18 January 2023; accepted 4 August 2023; published 21 August 2023)

The interaction between light and mechanical vibrations in a cavity is often exploited to produce higher-order sidebands (HOSs) or combs, which are used in optical communication networks and spectroscopy, among other things. Although an extensive study of optomechanically induced HOSs has been done, their proper control and manipulation using only continuous-wave (CW) laser drive are still to be explored. Here, we employ a mechanical parity-time- ( $\mathcal{PT}$ ) symmetric structure with optically induced gain and loss. It allows us to manipulate the flow of mechanical energies between the cavities, which has consequences on the optical response of the cavities. Based on our numerical investigations, we find that the higher-order optical sidebands start to emerge if  $\mathcal{PT}$  symmetry is broken. We precisely control the number of higher-order sideband lines by adjusting the coupling rate between the cavities with fixed drive power. In addition, we observe that the exceptional point (EP) induces the formation of two synchronized higher-order optical-sideband spectra, which opens a promising EP-based platform for the realization of optical readout of various mechanical synchronization phenomena, copies of the optomechanical frequency comb, sensing, and synchronization of remote clock time, among other things.

DOI: [10.1103/PhysRevA.108.023517](https://doi.org/10.1103/PhysRevA.108.023517)

### I. INTRODUCTION

Cavity optomechanics has become the subject of extensive study lately. The colocalization of the optical and mechanical modes in an optomechanical (OM) cavity has produced many interesting outcomes ranging from classical to quantum phenomena [1]. One of them is self-sustained mechanical oscillations [2,3] in the cavity, provided we drive the cavity with a blue-detuned cw laser above a certain threshold level [4]. The increase in driving cw laser power [5] or the large amplitude of the self-sustained oscillation [6] increases the optomechanical nonlinearity and creates significant modulation in the intracavity-field-intensity evolution. As a result, we get higher-order sidebands (HOSs) or combs in the optical spectrum with frequency line spacing decided by the mechanical resonance frequency. Miri *et al.* [7] showed that the formation of such a HOS or comb in an OM cavity is analogous to cascaded four-wave mixing in microresonator Kerr frequency combs [8]. A HOS can also be generated if one drives the cavity with a red-detuned pump laser and an external probe field because the beating of the cw pump laser with the probe at mechanical resonance frequency ensures coherent mechanical oscillations [9,10].

The optical HOS or comb has many exciting applications in spectroscopy [11], optical clocks [12], and other areas [13]. So the control and manipulation of an optomechanically induced HOS or comb are crucial in a low-power integrated structure. In the existing literature, the sidebands in the OM system

with pump-probe drive can be manipulated in many ways. For example, the relative phase and the power of the probe field can be utilized to manipulate the optical spectrum in the cavity [9]. The photon tunneling rate in coupled passive optical cavities also provides additional means to control the sidebands [14]. He [15] showed the use of active-passive coupled optical cavities in the  $\mathcal{PT}$ -symmetry structure to enhance the number of spectral lines. In general, the  $\mathcal{PT}$ -symmetry structure has been utilized in the field of optomechanics to show low-power phonon lasing [16], low-power chaos generation [17], enhanced optomechanically induced transparency (OMIT) [18], and mass sensing [19], among other things. Apart from these, hybrid atom-optomechanical systems have also been used to enhance and manipulate the sidebands [20]. But ample scope to investigate the proper control of sidebands when it comes to driving the cavity with a cw pump laser exists. Conventionally, it is done by increasing the cw laser drive power, but Djourjé *et al.* [21] utilized the dynamical attractors to manipulate the optical combs. Quadratic optomechanical coupling [22] and dissipation optomechanical coupling [23] are also being exploited in this regard.

The emergence of higher-order optical sidebands depends on the amplitude of the mechanical oscillation [24] in addition to driving power, where oscillations with higher amplitude result in more spectral lines [6]. In our study, we manipulate the amplitude of the oscillations to control the sidebands using only a cw pump-laser drive. This is achieved by using a mechanical  $\mathcal{PT}$ -symmetric structure with optically induced gain and loss [25]. In this system, we focus on tuning only the mechanical coupling rate to achieve control over the mechanical oscillation amplitude. Therefore, we are able to demonstrate a different way of invoking and controlling the

\*souvikjuetce95@kgpian.iitkgp.ac.in

†kapil.debnath@abdn.ac.uk

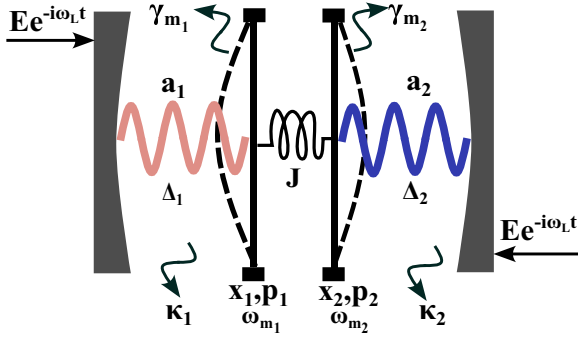


FIG. 1. Generic setup of two OM cavities (modeled by a Fabry-Pérot cavity where one end of the mirror is allowed to move freely) coupled mechanically (with coupling rate  $J$ ), forming a mechanical gain-loss OM system. The loss and gain of the mechanical resonators (with dimensionless position  $x_{1,2}$ , dimensionless momentum  $p_{1,2}$ , resonance frequency  $\omega_{m_{1,2}}$ , and decay rate  $\gamma_{m_{1,2}}$ ) are achieved by driving the cavity with red-detuned ( $\Delta_1 < 0$ ) and blue-detuned ( $\Delta_2 > 0$ ) cw lasers, respectively.

sidebands, contrary to the conventional way of adjusting the driving power. We also study the role of breaking the  $\mathcal{PT}$  symmetry to generate a HOS in a deterministic manner. In addition, we explore how the mechanical resonators with non-degenerate resonance frequency show collective behavior to produce synchronized optical HOSs. In the existing literature, the collective phenomena in OM systems are used for various classical and quantum synchronization purposes [26–28]. The synchronization process in our study is understanding the impact of an exceptional point (EP) on producing two wideband spectra with similar spectral envelopes.

This paper is organized in the following manner. In Sec. II, we show the mathematical model and the semiclassical dynamical equations in our coupled OM system. In Sec. III, we explore the mechanical  $\mathcal{PT}$ -symmetry optomechanical system, discussing the mechanical dynamics and its effect on intracavity intensity. In Sec. IV, we study the synchronization between the two optical HOSs in the cavities. Last, we summarize our work in Sec. V.

## II. MATHEMATICAL MODEL AND DYNAMICAL EQUATIONS

The system, as shown in Fig. 1, consists of two optomechanical cavities with mechanical coupling. The Hamiltonian of the whole system can be represented as the sum of individual optomechanical cavity terms (including the drive term) and the mechanical coupling term (assuming  $\hbar = 1$ ):

$$H_{\text{om}_j} = \omega_{c_j} \hat{a}_j^\dagger \hat{a}_j + \frac{\omega_{m_j}}{2} (\hat{x}_j^2 + \hat{p}_j^2) + g_{0_j} \hat{a}_j^\dagger \hat{a}_j \hat{x}_j + (E_j \hat{a}_j^\dagger e^{-i\omega_L t} + \text{H.c.}), \quad (1a)$$

$$H_{\text{coup}} = -J \hat{x}_1 \hat{x}_2, \quad (1b)$$

$$H_{\text{total}} = H_{\text{om}_1} + H_{\text{om}_2} + H_{\text{coup}}. \quad (1c)$$

The subscripts  $j = 1, 2$  indicate the two cavities, labeled cavity 1 and cavity 2, respectively.  $\hat{a}_j^\dagger$  and  $\hat{a}_j$  are the creation and destruction operators of the photons, respectively. Here,  $\hat{x}_j$  and  $\hat{p}_j$  are the dimensionless position and momentum

TABLE I. Parameters in the coupled OM system.

| Symbol                                       | Meaning                          |
|--|----------------------------------|
| $E_{1,2}$                                    | Driving strength of the laser    |
| $\kappa_{1,2}$                               | Optical cavity decay rates       |
| $\gamma_{m_{1,2}}$                           | Mechanical cavity decay rates    |
| $\omega_L$                                   | Driving laser frequency          |
| $\omega_{m_{1,2}}$                           | Mechanical resonance frequencies |
| $\omega_{c_{1,2}}$                           | Optical resonance frequencies    |
| $\Delta_{1,2} = \omega_L - \omega_{c_{1,2}}$ | Detuning of the laser            |
| $J$  | Mechanical coupling rate         |
| $g_{0_{1,2}}$                                | Optomechanical coupling rate     |

operators of the mechanical resonators, respectively. The details of the other parameters are given in Table I. Since we study the dynamics of the mean values of the operators, we ignore the fluctuations present in the system. Using the mean-field approximation, i.e.,  $\langle \hat{a}_j \hat{x}_j \rangle = \langle \hat{a}_j \rangle \langle \hat{x}_j \rangle$ , the dynamical equations of the mean values of operators ( $x_j \equiv \langle \hat{x}_j \rangle$ ,  $p_j \equiv \langle \hat{p}_j \rangle$ , and  $a_j \equiv \langle \hat{a}_j \rangle$ ) of the system in the rotating frame of the driving laser are written as [1,6,29]

$$\frac{da_j}{dt} = -i(\Delta_j + g_{0_j} x_j) a_j - \frac{\kappa_j}{2} a_j + E_j, \quad (2a)$$

$$\frac{dx_j}{dt} = \omega_{m_j} p_j, \quad (2b)$$

$$\frac{dp_j}{dt} = -\omega_{m_j} x_j - \frac{\gamma_{m_j}}{2} p_j + J x_{3-j} + g_{0_j} |a_j|^2. \quad (2c)$$

Equations (2) are coupled and nonlinear in nature. We evaluate the equations through numerical simulations since exact analytical derivations are difficult. Correspondingly, the steady-state expressions of the dynamical variables are written as

$$\bar{a}_j = \frac{E_j}{i(\Delta_j + g_{0_j} \bar{x}_j) + \frac{\kappa_j}{2}}, \quad (3a)$$

$$\bar{p}_j = 0, \quad (3b)$$

$$\omega_{m_j} \bar{x}_j = J \bar{x}_{3-j} + g_{0_j} |\bar{a}_j|^2. \quad (3c)$$

We made certain assumptions in the parameters in Eqs. (1)–(3). The mechanical cavities are degenerate, i.e.,  $\omega_{m_1} = \omega_{m_2} = \omega_m$ . We provide identical driving power  $E_1 = E_2 = E$  to the cavities. The decay rates and optomechanical coupling rates are identical, i.e.,  $\kappa_1 = \kappa_2 = \kappa$  and  $g_{0_1} = g_{0_2} = g_0$ . The detunings are in resonance with the mechanical resonance frequency, i.e.,  $-\Delta_1 = \Delta_2 = \omega_m$ .

## III. FORMATION OF HIGHER-ORDER OPTICAL SIDEBANDS

In this section, we study the temporal mechanical dynamics in a mechanical  $\mathcal{PT}$ -symmetric optomechanical configuration, followed by its effect on the optical response of the cavities.

### A. Mechanical $\mathcal{PT}$ -symmetry configuration

The conditions of mechanical  $\mathcal{PT}$  symmetry are obtained by adiabatically eliminating the optical modes where the effective optomechanical coupling  $G_{1,2} = g_0 a_{1,2}$  and

intrinsic decay rates  $\gamma_{m_{1,2}}$  are assumed to be weaker than  $\kappa$ , i.e.,  $\{G_{1,2}, \gamma_{m_{1,2}}\} \ll \kappa$ . Thus, the effective non-Hermitian Hamiltonian is written as [30]

$$H_{\text{eff}} = [(\omega_m - \delta\omega_{m_1}) - i\gamma_{\text{eff}_1}] \hat{b}_1^\dagger \hat{b}_1 + [(\omega_m + \delta\omega_{m_2}) + i\gamma_{\text{eff}_2}] \hat{b}_2^\dagger \hat{b}_2 - J(\hat{b}_1 \hat{b}_2^\dagger + \hat{b}_1^\dagger \hat{b}_2). \quad (4)$$

Here, the  $\hat{x}_j$  and  $\hat{p}_j$  operators of the mechanical resonators are written in terms of phonon creation ( $\hat{b}_j^\dagger$ ) and destruction ( $\hat{b}_j$ ) operators, where  $\hat{x}_j = \frac{\hat{b}_j + \hat{b}_j^\dagger}{\sqrt{2}}$  and  $\hat{p}_j = \frac{\hat{b}_j - \hat{b}_j^\dagger}{i\sqrt{2}}$ . After the elimination of the optical modes, the effective resonance frequency of mechanical resonators in cavities 1 and 2 becomes  $\omega_m \mp \delta\omega_{m_{1,2}}$ , while the effective decay (gain) rate becomes  $\gamma_{\text{eff}_1} = \gamma_{\text{opt}_1} + \gamma_{m_1}$  ( $\gamma_{\text{eff}_2} = \gamma_{\text{opt}_2} - \gamma_{m_2}$ ) [25,30,31]. The  $\delta\omega_{m_{1,2}}$  and  $\gamma_{\text{opt}_{1,2}}$  terms are the optomechanically modified terms [32], and at  $|\Delta_{1,2}| \sim \omega_m$ ,  $\gamma_{\text{opt}_{1,2}}$  is written as [33,34]

$$\gamma_{\text{opt}_{1,2}} = \frac{64g_0^2 |\bar{a}_{1,2}|^2 \omega_m^2}{\kappa(\kappa^2 + 16\omega_m^2)}. \quad (5)$$

The coupling rate  $J$  is assumed to be weaker, i.e.,  $J \ll \omega_m$ , and the interaction term in Eq. (1b) is written in the form of  $-J(\hat{b}_1 \hat{b}_2^\dagger + \hat{b}_1^\dagger \hat{b}_2)$  under the rotating-wave approximation. Applying  $\mathcal{P}$  transformation ( $i \leftrightarrow -i$ ,  $\hat{b}_1 \leftrightarrow -\hat{b}_2$ ,  $\hat{b}_1^\dagger \leftrightarrow -\hat{b}_2^\dagger$ ) and  $\mathcal{T}$  transformation ( $i \leftrightarrow -i$ ,  $\hat{b}_j \leftrightarrow \hat{b}_j$ ,  $\hat{b}_j^\dagger \leftrightarrow \hat{b}_j^\dagger$ ) to Eq. (4), we can show that  $[H_{\text{eff}}, \mathcal{PT}] = 0$  under the following conditions:  $\delta\omega_{m_j}$  is negligible ( $\delta\omega_{m_j} \ll \omega_m$ ), and  $\gamma_{\text{eff}_1} = \gamma_{\text{eff}_2}$ . Equivalently, in terms of  $\hat{x}$  and  $\hat{p}$  operators,  $\mathcal{P}$  transformation includes  $i \leftrightarrow -i$ ,  $\hat{x}_1 \leftrightarrow -\hat{x}_2$ , and  $\hat{p}_1 \leftrightarrow -\hat{p}_2$ , and  $\mathcal{T}$  transformation includes  $i \leftrightarrow -i$ ,  $\hat{x}_j \leftrightarrow \hat{x}_j$ , and  $\hat{p}_j \leftrightarrow -\hat{p}_j$  [35,36]. The mentioned strict conditions of  $\mathcal{PT}$  symmetry can be relaxed and are applicable for cases in which the effective decay rates are unequal,  $\gamma_{\text{eff}_1} \neq \gamma_{\text{eff}_2}$  [30,37]. The matrix representation of Eq. (4) is written as

$$H_{\text{eff}} = \begin{pmatrix} \hat{b}_1^\dagger & \hat{b}_2^\dagger \end{pmatrix} \begin{pmatrix} \omega_m - i\gamma_{\text{eff}_1} & -J \\ -J & \omega_m + i\gamma_{\text{eff}_2} \end{pmatrix} \begin{pmatrix} \hat{b}_1 \\ \hat{b}_2 \end{pmatrix}, \quad (6)$$

where the eigenfrequencies of the corresponding mechanical supermodes  $\hat{b}_1 \pm \hat{b}_2$  are calculated as

$$\omega_{\pm} = \omega_m - i \frac{\gamma_{\text{eff}_1} - \gamma_{\text{eff}_2}}{4} \pm \sqrt{\chi}, \quad (7)$$

where  $\chi$  is given by

$$\chi = J^2 - \left( \frac{\gamma_{\text{eff}_1} + \gamma_{\text{eff}_2}}{4} \right)^2. \quad (8)$$

The system respects  $\mathcal{PT}$  symmetry if  $\chi > 0$ , in which the real part of the eigenfrequencies is split by the amount  $2\sqrt{\chi}$ . The  $\mathcal{PT}$  symmetry breaks down if  $\chi < 0$ ; in this regime, the eigenfrequencies of the two supermodes coalesce onto each other, and the supermodes experience either gain or loss. The transition from the  $\mathcal{PT}$  phase to the broken  $\mathcal{PT}$  phase occurs at  $\chi = 0$ , i.e.,  $J = \frac{\gamma_{\text{eff}_1} + \gamma_{\text{eff}_2}}{4}$ , which is known as the exceptional point.

In our study, we keep the effective rates, i.e.,  $\gamma_{\text{eff}_1}$  and  $\gamma_{\text{eff}_2}$ , fixed (or, equivalently, the driving power is kept fixed) and vary the mechanical coupling rate  $J$ . Since the driving

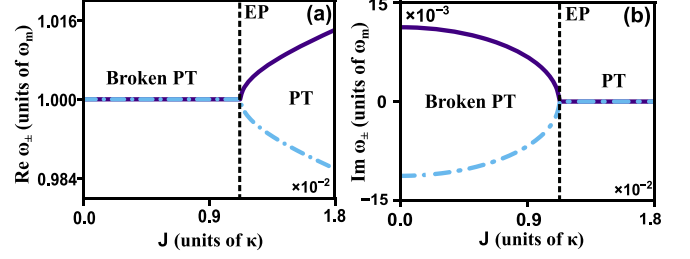


FIG. 2. (a) Real and (b) imaginary parts of the eigenfrequencies  $\omega_+$  (solid line) and  $\omega_-$  (dash-dotted line) in which an EP (dashed vertical line) occurs at  $J = \frac{\gamma_{\text{eff}_1} + \gamma_{\text{eff}_2}}{4} = 1.1 \times 10^{-2} \kappa$ .

strength  $E$  is the same for both the cavities,  $\gamma_{\text{opt}_1} \approx \gamma_{\text{opt}_2} = \gamma_{\text{opt}}$ , and we choose  $\gamma_{\text{opt}} = 0.02\kappa$ . The intrinsic decay rate  $\gamma_{m_1}$  of the resonator in cavity 1 is made higher (more dissipative) than the other, i.e.,  $\gamma_{m_1} = 5 \times 10^{-3}\kappa$  and  $\gamma_{m_2} = 10^{-4}\kappa$ , such that  $\gamma_{\text{eff}_1} = 2.5 \times 10^{-2}\kappa$  and  $\gamma_{\text{eff}_2} \approx 2 \times 10^{-2}\kappa$ . We choose  $\gamma_{\text{eff}_1} > \gamma_{\text{eff}_2}$  to provide decaying dynamics in the  $\mathcal{PT}$  phase, and its further significance is discussed in the next subsection. The decay rates are chosen to be on the order of  $10^{-2}\kappa$ , and we vary the mechanical coupling rate on the same order. We choose  $\omega_m = 10\kappa$  to operate the cavities in the resolved regime such that  $\delta\omega_{m_j}$  is negligible [33,34] and the optomechanical coupling rate is set to  $g_0 = 10^{-3}\kappa$ . The values of the parameters mentioned here can be achieved in experiments [38,39]. Figures 2(a) and 2(b) show the real and imaginary parts of the eigenfrequencies, respectively, obtained with Eqs. (7) and (8). The  $\mathcal{PT}$ -symmetric phase is observed at a coupling rate larger than  $\frac{\gamma_{\text{eff}_1} + \gamma_{\text{eff}_2}}{4}$ , i.e.,  $J > \frac{\gamma_{\text{eff}_1} + \gamma_{\text{eff}_2}}{4} = 1.1 \times 10^{-2}\kappa$ , where  $\text{Re } \omega_{\pm}$  are split about  $\omega_m$ . Lowering the coupling rate below  $\frac{\gamma_{\text{eff}_1} + \gamma_{\text{eff}_2}}{4}$ , i.e.,  $J < \frac{\gamma_{\text{eff}_1} + \gamma_{\text{eff}_2}}{4} = 1.1 \times 10^{-2}\kappa$ , will break the  $\mathcal{PT}$  phase, where one supermode experiences loss while the other experiences gain [see Fig. 2(b)] and  $\text{Re } \omega_{\pm}$  overlap each other. The transition between the two phases occurs through the EP at the critical coupling rate  $J = J_{\text{critical}} = 1.1 \times 10^{-2}\kappa$ . The analytical treatment to obtain  $J_{\text{critical}}$  works consistently with numerical simulations (which will be performed in the next section) by operating  $\gamma_{\text{opt}_{1,2}} \lesssim 0.5\kappa$ . For simplicity, we did not consider the effect of multiple EPs, which would be prevalent in this type of system if we operate  $\gamma_{\text{opt}_{1,2}} > 0.5\kappa$ . Because fixing  $\gamma_{\text{opt}_{1,2}}$  at a high value requires larger driving power, the combination of strong optomechanical nonlinearity and a larger mechanical coupling rate would invoke multiple EPs, as is evident in [40].

## B. Temporal mechanical dynamics and stability analysis

We solved Eq. (2) using the Runge-Kutta method to obtain the mechanical dynamics at various regimes with the initial conditions of all the dynamical variables set to zero. The numerical analysis includes the optical modes instead of adiabatically eliminating them, as done in Sec. III A. We require the value of driving amplitude  $E$  under steady-state conditions to perform the numerical analysis. Using the parameters in the previous section, we extract the steady intracavity intensity  $|\bar{a}_j|^2$  from Eq. (5), which is substituted in Eq. (3). Considering weak optomechanical interactions, we can safely ignore the term  $g_0 \bar{x}_j$  in Eq. (3), and thereby, we obtain the driving

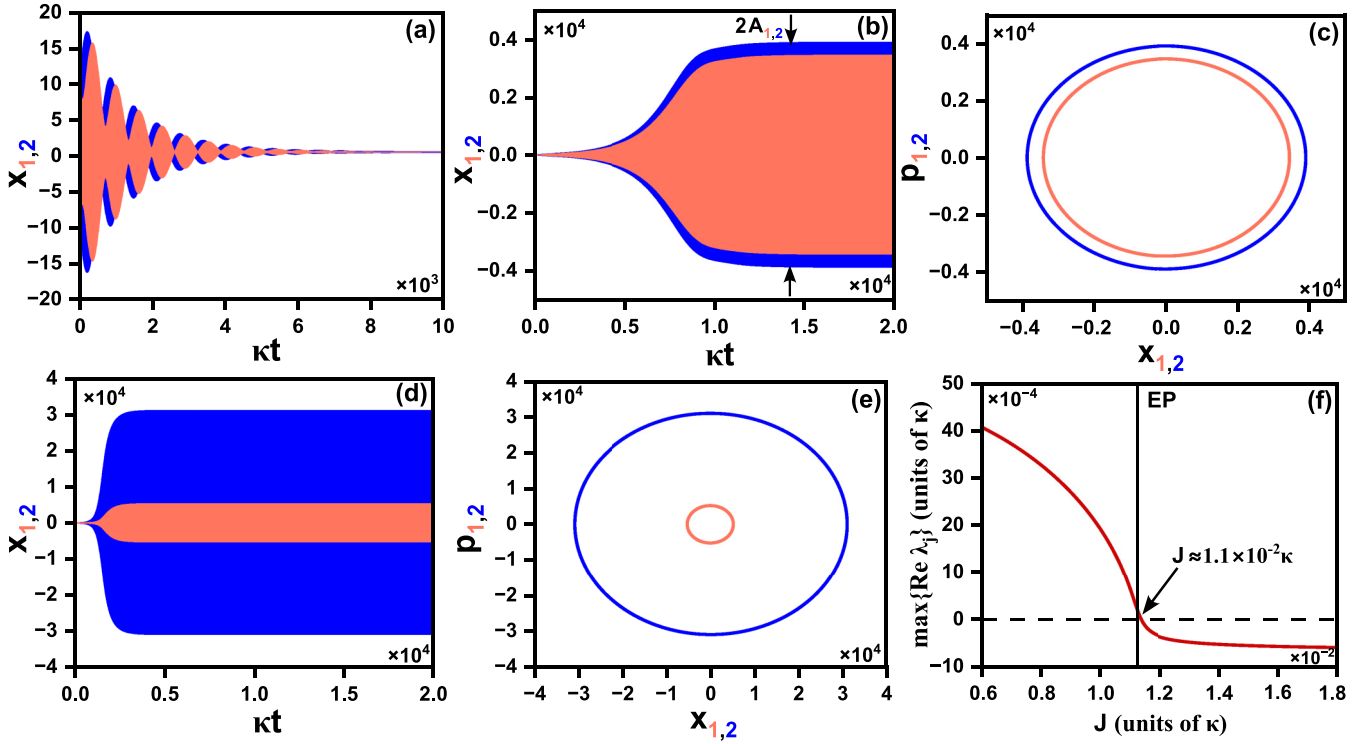


FIG. 3. (a) The dynamics of two mechanical resonators,  $x_1$  (orange lines) and  $x_2$  (blue lines), with decaying oscillations in the  $\mathcal{PT}$  phase at  $J = 1.5 \times 10^{-2}\kappa (=1.4 \frac{\gamma_{\text{eff}_1} + \gamma_{\text{eff}_2}}{4})$ . (b) The mechanical dynamics with steady amplitude of oscillations  $A_{1,2}$  at the EP for  $J = 1.1 \times 10^{-2}\kappa (= \frac{\gamma_{\text{eff}_1} + \gamma_{\text{eff}_2}}{4})$ . (c) The mechanical trajectories of resonator 1 (orange lines) and resonator 2 (blue lines) in the phase space, showing limit cycles at the EP. (d) The mechanical dynamics in the broken  $\mathcal{PT}$  phase at  $J = 0.2 \times 10^{-2}\kappa (= 0.18 \frac{\gamma_{\text{eff}_1} + \gamma_{\text{eff}_2}}{4})$ . (e) The mechanical trajectories in the phase space in the broken  $\mathcal{PT}$  regime. (f) The stability analysis showing the transition between stable and unstable regions close to the EP.

strength  $E \approx 709\kappa$ . Therefore, the parameters  $\omega_m$ ,  $|\Delta_{1,2}|$ ,  $g_0$ ,  $\gamma_{m_1}$ ,  $\gamma_{m_2}$ , and  $E$  of the numerical simulation are set as  $10\kappa$ ,  $10\kappa$ ,  $10^{-3}\kappa$ ,  $5 \times 10^{-3}\kappa$ ,  $10^{-4}\kappa$ , and  $709\kappa$ . Figure 3(a) shows the mechanical dynamics in the  $\mathcal{PT}$  phase for the chosen coupling rate of  $J = 1.5 \times 10^{-2}\kappa (=1.4 \times \frac{\gamma_{\text{eff}_1} + \gamma_{\text{eff}_2}}{4})$ . Here, the choice of coupling rate  $J$  is for representational purposes, and  $J$  can be any value greater than  $\frac{\gamma_{\text{eff}_1} + \gamma_{\text{eff}_2}}{4}$ , which would show the same dynamics. We observe periodic amplitude variation dynamics in both resonators, which indicates a strong exchange of mechanical energy between the resonators, and the hybridized mechanical modes  $\hat{b}_1 \pm \hat{b}_2$  with energy levels decided by  $\text{Re } \omega_+$  and  $\text{Re } \omega_-$  exhibit a gap. In this regime, the effective loss of the mechanical resonator in cavity 1 overcompensates the effective gain of the resonator in cavity 2, and thereby, the mechanical dynamics decays at the rate  $(\gamma_{\text{eff}_1} - \gamma_{\text{eff}_2})/4 \approx 1.3 \times 10^{-3}\kappa$ . Lowering the coupling rate towards the EP at  $J = 1.1 \times 10^{-2}\kappa (= \frac{\gamma_{\text{eff}_1} + \gamma_{\text{eff}_2}}{4})$  gives rise to self-sustained oscillation with steady amplitude  $A_j$  in both mechanical resonators, as shown in Fig. 3(b). Here, the energy levels of the hybridized mode given by  $\text{Re } \omega_{\pm}$  coalesce onto each other (i.e.,  $\text{Re } \omega_{\pm} = \omega_m$ ), triggering spontaneous localization of the mechanical energies in the resonators. In other words, the mechanical coupling reduces to the critical value where there is no longer an exchange of mechanical energies, and the effective loss in one mechanical resonator cannot compensate for the effective gain in another. As a result, the mechanical oscillation in the second resonator is

amplified. The first resonator with effective loss also experiences amplification since coupling with the second resonator is finite. As the driving strength  $E$  induces strong optomechanical nonlinearity in both cavities, the growth of oscillations in the resonators is stabilized and forms limit cycles, as shown in Fig. 3(c). The value of the amplitude  $A_j$  depends on how the incident optical power balances the mechanical dissipation in cavity 2 [21,24] and the amount of mechanical coupling to cavity 1. Intuitively, one would expect the limit cycles in both resonators to have the same amplitude, but the first resonator has a slightly lower amplitude [see Fig. 3(c)] because a fraction of the local mechanical energy ( $\sim A_1^2$ ) is lost in the environment through the higher effective decay rate  $\gamma_{\text{eff}_1}$ . Figure 3(d) shows the dynamics in the broken  $\mathcal{PT}$  phase at a lower coupling rate of  $J = 0.2 \times 10^{-2}\kappa (= 0.18 \frac{\gamma_{\text{eff}_1} + \gamma_{\text{eff}_2}}{4})$ , where the oscillations quickly grow to settle into steady amplitude. From the mechanical phase portrait in Fig. 3(e), we observe that  $A_2$  has a significantly higher value than  $A_1$  the other since a lower amount of coupling would result in more confinement of mechanical energy in the second resonator.

We performed a linear stability analysis to relate the instability in the system to the growth of mechanical oscillation in the resonators after breaking the symmetry conditions. The nonlinear coupled dynamical equation (2) can be linearized by considering the perturbation of the dynamical variables around a strong average value, i.e.,  $o = \bar{o} + \delta o$  (where  $o = a_j, x_j, p_j$ ). Therefore, the linearized form of the dynamical

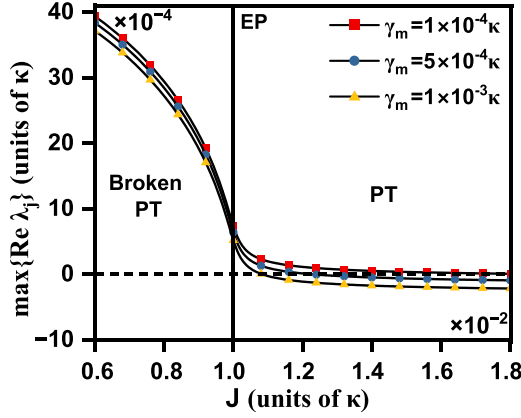


FIG. 4. Possible realization of the system with a balanced effective gain-loss condition. Lower decay rates of the order of  $10^{-4}\kappa$  give rise to instability in the  $\mathcal{PT}$  phase.

equations without noise is written as

$$\frac{d\Psi}{dt} = M\Psi, \quad (9)$$

where  $\Psi = (\delta a_1, \delta a_1^*, \delta a_2, \delta a_2^*, \delta x_1, \delta p_1, \delta x_2, \delta p_2)^T$  and the  $8 \times 8$  matrix  $M$  is given in Appendix A. The stability condition of the system can be explicitly obtained through the Routh-Hurwitz criterion [41], but it would be cumbersome to show here. So we numerically obtained the stability conditions of the system by observing the real parts of the eigenvalues ( $\lambda_j/\kappa$ ,  $j = 1, 2, \dots, 8$ ) of  $M$ . The system loses its stability if any of the real parts of  $\lambda_j$  become positive. Figure 3(f) shows the maximum of the eigenvalues  $\lambda_j/\kappa$  of  $M$  with the variation of the mechanical coupling rate, where the system becomes unstable in the regime  $J \leq 1.1 \times 10^{-2}\kappa = \frac{\gamma_{\text{eff}_1} + \gamma_{\text{eff}_2}}{4}$ . Thus, by breaking the  $\mathcal{PT}$  symmetry through the EP, the system loses its stability. The instability caused by breaking the symmetry will result in the growth of mechanical oscillations (ultimately towards limit cycles), as confirmed by the mechanical dynamics obtained numerically. Consequently, the limit cycles will result in optical-sideband formation, as we will discuss in the next section.

The intrinsic decay rates of the mechanical resonators can be chosen to be equal,  $\gamma_{m_1} = \gamma_{m_2} = \gamma_m$ , at lower values ( $\gamma_m \lesssim 0.1\gamma_{\text{opt}}$ ), such that we can have balanced effective gain and loss, i.e.,  $\gamma_{\text{eff}_1} = \gamma_{\text{eff}_2} \approx \gamma_{\text{opt}}$ . But the transition point between the stable and unstable regimes does not happen close to the EP. As shown in Fig. 4, the unstable region persists in the  $\mathcal{PT}$  phase for lower values of decay rates, which may give rise to finite oscillations. So operating under balanced gain-loss conditions suffers from stability issues in the  $\mathcal{PT}$  phase. Increasing  $\gamma_m$  makes the transition point move towards the EP, and  $\gamma_{\text{eff}_1}$  ( $= \gamma_{\text{opt}} + \gamma_m$ ) starts to dominate over  $\gamma_{\text{eff}_2}$  ( $= \gamma_{\text{opt}} - \gamma_m$ ). We choose  $\gamma_{m_1} > \gamma_{m_2}$  ( $\gamma_{\text{eff}_1} > \gamma_{\text{eff}_2}$ ) from a practical realization point of view because engineering perfectly balanced  $\gamma_m$  can be difficult.

### C. Intensity dynamics and Fourier spectra

The limit cycles of the mechanical resonator in an optomechanical cavity will lead to the formation of optical

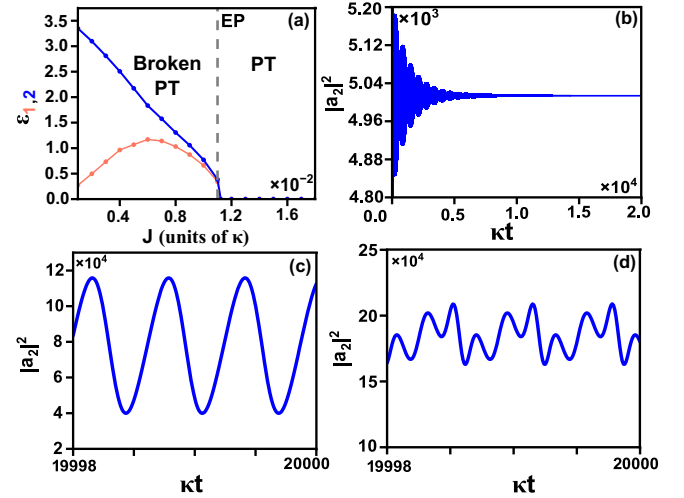


FIG. 5. (a) Normalized oscillation amplitudes  $\varepsilon_1$  (orange line with dots) and  $\varepsilon_2$  (blue line with dots) with the variation of the mechanical coupling rate  $J$ . (b)–(d) The steady evolution of the intracavity photon number  $|a_2|^2$  for the  $\mathcal{PT}$  phase ( $J = 1.4 \frac{\gamma_{\text{eff}_1} + \gamma_{\text{eff}_2}}{4}$ ), EP ( $J = \frac{\gamma_{\text{eff}_1} + \gamma_{\text{eff}_2}}{4}$ ), and broken  $\mathcal{PT}$  phase ( $J = 0.18 \frac{\gamma_{\text{eff}_1} + \gamma_{\text{eff}_2}}{4}$ ), respectively.

higher-order sidebands with sufficient drive power and a high amplitude of the mechanical oscillations [6,7]. The phenomenon is related to the cascaded interaction of scattered light (photons) in the cavity with sustained mechanical motions (phonons). The analytical solution of the intracavity light field is written as an infinite sum of frequency components spaced by integer multiples of mechanical resonance frequency  $\pm k\omega_m$  ( $k = 0, 1, 2, \dots$ ) if we assume  $x_j(t) = \varepsilon_j \cos(\omega_m t)$  (where  $\varepsilon_j = \frac{g_0 A_j}{\omega_m}$  is the normalized amplitude) [24]:

$$a_j(t) = e^{i\varepsilon_j \sin(\omega_m t)} \sum_{k=-\infty}^{\infty} a_j^k e^{ik\omega_m t}. \quad (10)$$

In terms of  $\varepsilon_j$ ,  $a_j^k \propto J_k(-\varepsilon_j)$ , where  $J_k$  is the  $k$ th-order Bessel function of the first kind. We are able to achieve continuous control of the amplitude of oscillation  $A_j$  (or  $\varepsilon_j$ ) by tuning  $J$  as shown in Fig. 5(a), which directly impacts the strength of the intracavity field at different sidebands. In Eq. (10), the change in normalized amplitude  $\varepsilon_j$  with the coupling  $J$  is implicitly present, i.e.,  $\varepsilon_j = \varepsilon_j(J)$ . We have a finite and varying  $\varepsilon_j$  if we break the  $\mathcal{PT}$  phase. We observe a continuous increase of  $\varepsilon_2$  towards the value of 3.2 (i.e., for the case of  $J = 0$ ) as we reduce the coupling, while  $\varepsilon_1$  decreases towards zero. As mentioned in Sec. III B, this happens because of stronger confinement of mechanical energy in the second mechanical resonator with lower coupling strength. For the remainder of this section, we focus on only the effect of mechanical oscillations on the optical response of cavity 2. Figures 5(b)–5(d) show the evolution of the intracavity photon number  $|a_2|^2$  for different conditions. In the  $\mathcal{PT}$  phase,  $|a_2|^2$  decays to a steady value of around  $5 \times 10^3$ . Once the EP is reached, the dynamical back-action of the finite mechanical oscillation modulates the intracavity optical intensity. The intensity is further modulated in the broken  $\mathcal{PT}$  phase due to high  $\varepsilon_2$ .

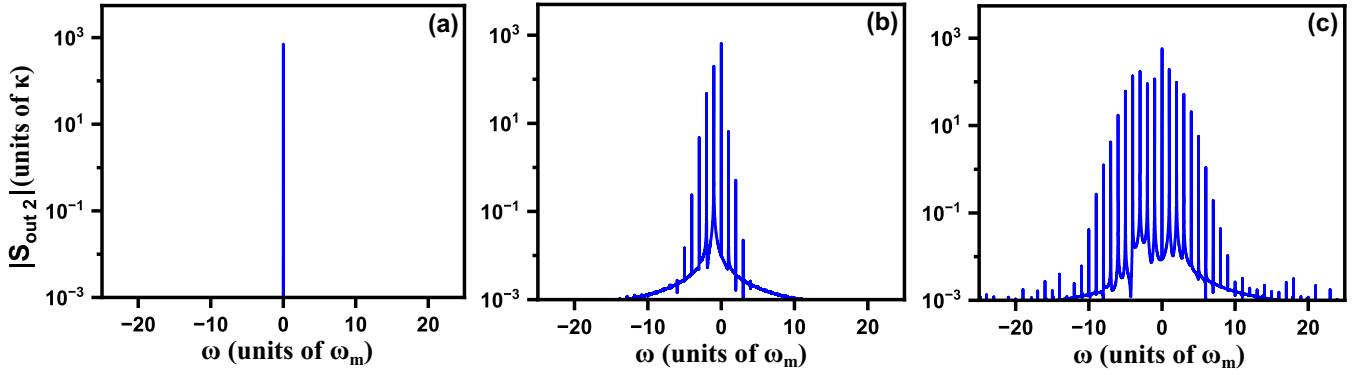


FIG. 6. The output optical spectrum  $|S_{\text{out}_2}|$  of cavity 2 corresponding to the (a)  $\mathcal{PT}$  phase ( $J = 1.4 \frac{\gamma_{\text{eff}_1} + \gamma_{\text{eff}_2}}{4}$ ), (b) exceptional point ( $J = \frac{\gamma_{\text{eff}_1} + \gamma_{\text{eff}_2}}{4}$ ), and (c) broken  $\mathcal{PT}$  phase ( $J = 0.18 \frac{\gamma_{\text{eff}_1} + \gamma_{\text{eff}_2}}{4}$ ).

The output light field from the cavities is obtained from input-output formalism [42], i.e.,  $a_{\text{out}_j}(t) = E(t) - \kappa a_j(t)$ . We obtained the output optical spectrum by taking the Fourier transform of the output field, i.e.,  $S_{\text{out}_j}(\omega) \propto \int_{-\infty}^{\infty} a_{\text{out}_j}(t) e^{-i\omega t} dt$ . Figure 6 shows the output optical spectrum from cavity 2 under different conditions. We did Fourier transform the steady response of  $a_{\text{out}_2}(t)$  numerically to show the spectrum of cavity 2. As our study is in the rotating frame of the driving laser, the actual spectrum is shifted by  $\omega_L$ . In the  $\mathcal{PT}$  phase shown in Fig. 6(a), the spectrum has no sidebands because the system is in a steady state with damped oscillations. We see a sudden transition in the nature of the output spectrum at the EP in Fig. 6(b) because the sidebands appear with a frequency spacing of  $\omega_m$ . This happens because of the emergence of the limit cycle, as discussed earlier. Figure 6(c) shows a significant increase in the spectral lines in the broken  $\mathcal{PT}$  phase because the increased confinement of mechanical energy leads to limit cycles with higher amplitude. In our analysis, we did not consider any source of noise or fluctuations in the system that contributes to the linewidth of the sidebands because we are interested in the center line of the sidebands. Since the intracavity field acquires strengthened higher-order frequency components when the symmetry is broken (as is evident from the intensity dynamics in Fig. 5), we can write the output field in the form of Eq. (10) as  $a_{\text{out}_j}(t) = \sum_{k=-\infty}^{\infty} r_j^k e^{ik\omega_m t}$  ( $k = 0, \pm 1, \pm 2, \dots$ ). So the spectrum obtained in Fig. 6 is equivalent to taking the Fourier transform of  $a_{\text{out}_j}(t) = \sum_{k=-\infty}^{\infty} r_j^k e^{ik\omega_m t}$ . Hence, we are able to invoke higher-order sidebands by breaking the  $\mathcal{PT}$  symmetry.

Thus, in our study, we do not require any combination of pump-probe lasers or any adjustment of the cw driving power to achieve control of the sidebands, but rather, we tune only the coupling rate. In the current literature, proper control and enhanced generation of HOSs are explored in active-passive and passive-passive coupled optical cavities or hybrid optomechanical systems. However, our investigation focuses on the generation of HOSs in the mechanical gain-loss optomechanical system, a previously unexplored aspect. This system presents a deterministic approach to generating and controlling HOSs by breaking  $\mathcal{PT}$  symmetry through the EP using a cw laser drive. One could also consider a mechanical gain-gain or loss-loss optomechanical system, but they do not provide proper control of HOSs (see Appendix B).

#### IV. SYNCHRONIZATION BETWEEN TWO SPECTRA

To this point, we have observed the output optical spectrum from cavity 2, but the sidebands will also emerge in the red-detuned cavity 1 since a finite oscillation amplitude  $\varepsilon_1$  exists in the broken-symmetry phase. We show, in this section, the output HOS exists in both the optical cavities in a “synchronized” manner. Here, we define synchronization subject to the fulfillment of the following conditions: (i) locking of the spectral peaks to a common frequency if any frequency mismatch exists and (ii) similarity of the spectral envelopes. Since the nature of the spectral envelopes is determined by  $\varepsilon_j$  [see Eq. (10)], the difference  $|\varepsilon_2 - \varepsilon_1|$  plays a deciding role in the synchronization process, as we will see later in this section.

We set the resonance frequencies in the mechanical resonators to be nondegenerate, i.e.,  $\omega_{m_1} \neq \omega_{m_2}$ , and substitute them in the matrix [see Eq. (6)] to obtain the new eigenvalues of the supermodes as

$$\omega_{\pm} = \frac{\omega_{m_1} + \omega_{m_2}}{2} - i \frac{\gamma_{\text{eff}_1} - \gamma_{\text{eff}_2}}{4} \pm \sqrt{J^2 + \left( \frac{\Delta\omega}{2} + i \frac{\gamma_{\text{eff}_1} + \gamma_{\text{eff}_2}}{4} \right)^2}, \quad (11)$$

where  $\Delta\omega = \omega_{m_2} - \omega_{m_1}$ .

Due to the presence of  $\Delta\omega$ , the system no longer respects  $\mathcal{PT}$  symmetry, and the degeneracy of the two supermodes is lifted near the EP. Employing nondegenerate resonators with a minor frequency mismatch presents a more practical scenario, as it can be challenging to engineer perfectly matched frequencies. We provide a map of the synchronized HOS regime in Fig. 7 in the parametric space of frequency deviation  $\Delta\omega$  and coupling rate  $J$ . We identify four regimes: (i) In the *steady state*, there are no sidebands in the regime because the mechanical oscillations in the cavity remain absent, and this regime exists in the higher mechanical coupling region. (ii) In the *intermediate state*, the mechanical oscillations start to grow, but it takes many time cycles to reach the stable limit cycle. (iii) In the *synchronized state*, the mechanical oscillations reach the limit cycles to produce synchronized HOSs with similar spectral envelopes. (iv) In the *asynchronized state*, the optical spectra in the cavities no longer remain

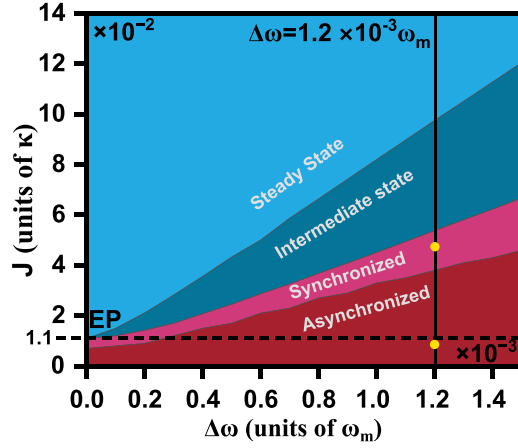


FIG. 7. Possible regimes in our system in the parameter space of resonance-frequency deviation  $\Delta\omega = \omega_{m_2} - \omega_{m_1}$  and mechanical coupling rate  $J$ . The synchronized regime moves away from the EP line as  $\Delta\omega$  increases.

synchronized because the spectral envelopes are vastly different, and this regime exists in the lower mechanical coupling region. The boundary between the steady-state and intermediate-state regimes is obtained with the linear stability analysis. The system goes into the intermediate state from the steady-state regime when one of the eigenvalues of the matrix  $M$  in Eq. (9) becomes positive, such that the mechanical oscillations start to grow, and the system becomes unstable. But the oscillations do not acquire limit cycles right away since the system goes into a sort of intermediate-state regime [43] before the two resonators with finite  $\Delta\omega$  oscillate with locked frequency. The higher-order sidebands are not fully formed in this regime. In the synchronized regime, the two resonators mutually synchronize themselves to oscillate with a locked frequency [40]. The amplitudes of the limit cycles are close enough to produce HOSs with similar spectral envelopes in both cavities. The boundary between the intermediate state and the synchronized regime can be described by analyzing the imaginary part of Eq. (11). We find that near the boundary  $\text{Im } \omega_+ \approx 0$  and in the synchronized regime  $\text{Im } \omega_+ > 0$ . The positive growth rate of one of the supermodes indicates that the oscillation in the resonators grows quickly to form limit cycles. Figure 8(a) shows  $\text{Im } \omega_{\pm}$  with the variation of the mechanical coupling rate where the higher-frequency deviation  $\Delta\omega$  results in higher separation between  $\text{Im } \omega_+$  and  $\text{Im } \omega_-$  near the EP. The plot of  $\text{Im } \omega_{\pm}$  is obtained by using the following expression:

$$\text{Im } \omega_{\pm} = -\frac{\gamma_{\text{eff}_1} - \gamma_{\text{eff}_2}}{4} \pm \sqrt{\frac{\eta^2 + (\Delta\omega \frac{\gamma_{\text{eff}_1} + \gamma_{\text{eff}_2}}{4})^2}{2}} - \eta, \quad (12)$$

where  $\eta = J^2 - (\frac{\gamma_{\text{eff}_1} + \gamma_{\text{eff}_2}}{4})^2 + (\frac{\Delta\omega}{2})^2$ . The expression is obtained explicitly by taking the imaginary part of Eq. (11). The plot of  $\text{Im } \omega_+$  in Fig. 8(b) determines at what mechanical coupling strength the growth rate of the supermode becomes positive. We observe that the critical mechanical coupling strength where  $\text{Im } \omega_+ = 0$  increases for higher  $\Delta\omega$ . Intuitively, we

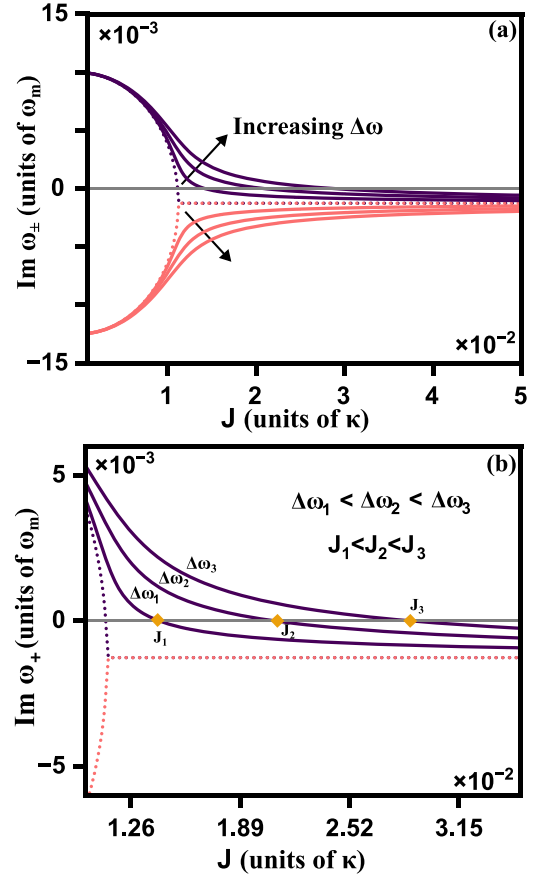


FIG. 8.  $\text{Im } \omega_{\pm}$  with the variation of mechanical coupling  $J$ , where the dotted lines are for the  $\mathcal{PT}$ -symmetric configuration when  $\Delta\omega = 0$ . (a) The degeneracy near the EP is lifted for  $\Delta\omega \neq 0$ , where the gap between  $\text{Im } \omega_+$  (violet solid curve) and  $\text{Im } \omega_-$  (orange solid curve) increases for larger  $\Delta\omega$ . (b) The critical coupling strength where  $\text{Im } \omega_+ = 0$  increases with increasing  $\Delta\omega$ .

explain this by saying that higher critical mechanical coupling strength is required to synchronize the resonators with a large resonance-frequency deviation. The asynchronized regime occurs at a lower mechanical coupling rate with a significant difference in the amplitude of oscillations, and the boundary line with the synchronized regime can be best described by comparing the intracavity intensity phase portraits. We choose a certain frequency shift, say,  $\Delta\omega = 1.2 \times 10^{-3} \omega_m$ , to observe the frequency spectrum in the synchronized and asynchronized regimes and explain in the later part of this section how we decided the boundary between synchronized and asynchronized regimes. The demarcation between the regimes determined through analytical methods closely aligns with the boundaries obtained by observing the dynamics and spectra numerically. We also observe from Fig. 7 that the synchronized regime deviates away from the EP towards a higher coupling region as  $\Delta\omega$  increases. Thus, the success of the deterministic method of synchronizing the two spectra by tuning the system towards the EP decreases.

We took points (shown by the yellow dots in Fig. 7) in the synchronized and asynchronized regimes at  $J = 4.5 \times 10^{-2} \kappa$  and  $J = 1 \times 10^{-2} \kappa$ , respectively, to observe the spectrum. Figure 9(a) shows the nature of the two output spectra in

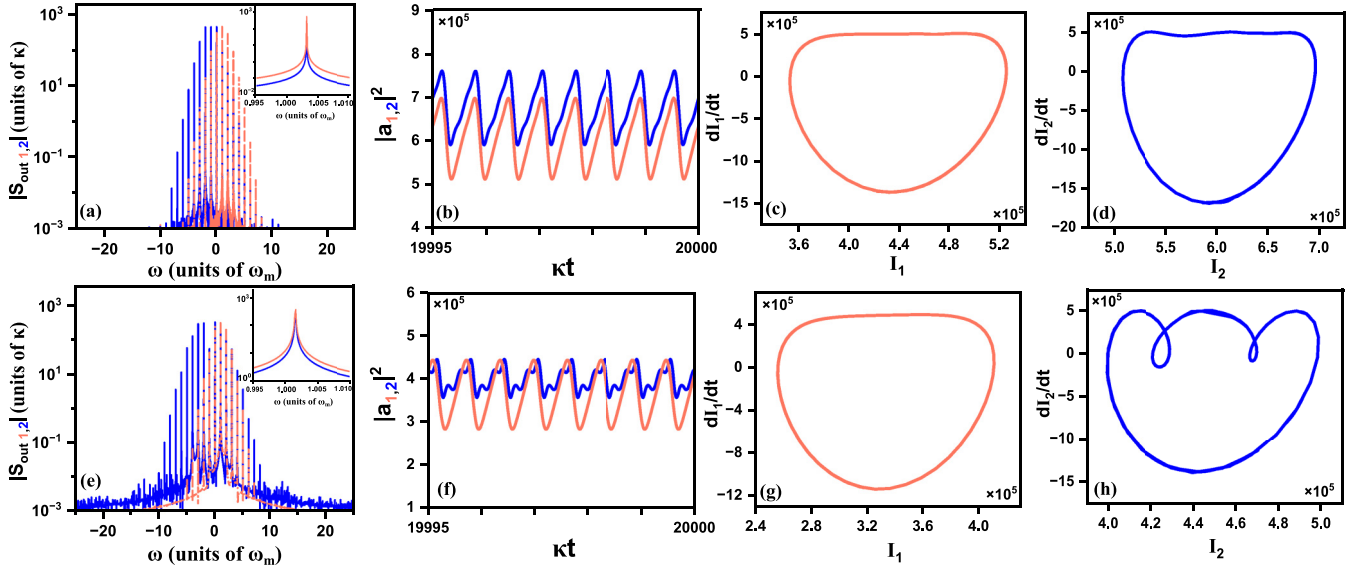


FIG. 9. Spectral profile and intracavity intensity of cavity 1 (orange) and cavity 2 (blue) in the synchronized and asynchronous regimes for  $\Delta\omega = 1.2 \times 10^{-3}\omega_m$ . (a) Similar spectral envelopes of the two output optical spectra in the synchronized regime ( $J = 4.5 \times 10^{-2}\kappa$ ), with the inset showing the first-order spectral component, coincide with each other at a frequency slightly offset from  $\omega = \omega_m$ . (b) The dynamics of the intracavity intensity of the two cavities in the synchronized regime, with the corresponding interpretation in phase space given in (c) and (d), where  $I_j = |a_j|^2$ . (e) Different spectral envelopes of the two output optical spectra in the asynchronous regime ( $J = 1 \times 10^{-2}\kappa$ ), with the inset showing the first-order frequency component. (f) The intracavity intensity dynamics in the asynchronous regime, with the corresponding interpretation in phase space given in (g) and (h).

the synchronized regime. We observe that the spectra have similar spectral envelopes, as the difference  $|\varepsilon_2 - \varepsilon_1|$  is not significant. Even though the spectral envelopes are similar, the lines for cavity 1 are more concentrated towards  $\omega > 0$  since the density of states of cavity 1 is concentrated at frequencies higher than the driving laser frequency  $\omega_L$ . On the other hand, cavity 2 has lines concentrated towards  $\omega < 0$  because the density of states is concentrated at frequencies lower than the driving laser frequency  $\omega_L$ . In addition, both the HOS spectra have the same uniform frequency spacing, with the inset in Fig. 9(a) showing a zoomed-out version of the first-order component around  $\omega = \omega_m$ . The amount of spacing is decided by the locked frequency at which the resonators oscillate. The locked frequency takes the value of the eigenfrequency of the upper supermode, i.e.,  $\text{Re } \omega_+$  (see Appendix C). It is interesting to see the nature of the evolution of the intracavity field intensity corresponding to it. We observe in Fig. 9(b) that the intensity in cavity 1 follows that of cavity 2 with the corresponding visualization in phase space given in Figs. 9(c) and 9(d). In the asynchronous regime, the nature of the spectrum envelope in both cavities becomes vastly different, as shown in Fig. 9(e). Even though the sidebands in both the spectra are locked at a common frequency, as shown in the inset in Fig. 9(e), cavity 2 has more spectral lines than cavity 1 since the difference  $|\varepsilon_2 - \varepsilon_1|$  become significant. As a result, the spectral envelope of cavity 2 becomes wider than that of cavity 1. These are also reflected in the intracavity intensity dynamics in Fig. 9(f), where the evolution of  $|a_2|^2$  becomes significantly different. The corresponding visualization in phase space is given in Figs. 9(g)–9(h), which provide us with a perfect way to determine the boundary between the synchronized and asynchronous regimes. The boundary is decided by the similarity between the two intracavity trajectories of the

cavities in phase space. The occurrence of HOSs in both the synchronized and asynchronous spectral regimes is attributed to the presence of limit cycles in the mechanical resonators, which oscillate with a certain locked frequency [40]. So the sidebands of the two cavities always coincide for both synchronized and asynchronous spectra, as shown in the insets in Figs. 9(a) and 9(e). Thus, for the asynchronous spectrum, only condition (i) for defining synchronization is satisfied. So, in our study, the amplitude of mechanical oscillations plays the deciding role in the synchronization process in which two spectra with similar envelopes are generated, and the impact of EP dominates for a very weak resonance-frequency shift. Hence, in addition to enabling control and deterministic generation of HOSs, the mechanical gain-loss optomechanical setup has the benefit of achieving synchronization of spectral envelopes by tuning the system near the EP.

## V. SUMMARY

In summary, we theoretically investigated the formation, control, and synchronization of optical-sideband spectra in weak mechanically coupled optomechanical cavities. The research yielded valuable insights into the intricate relationship between the mechanical gain-loss structure, optomechanical nonlinearity, and the generation of HOSs. This work was done with fixed cw driving laser power (i.e., the effective mechanical gain and loss rates were kept fixed) with varying mechanical coupling rate. We obtained the mechanical dynamics along with the corresponding effect on the evolution of intracavity intensity in different circumstances. Consequently, we found an abrupt emergence of HOSs in the optical spectrum by breaking the mechanical  $\mathcal{PT}$  symmetry. This happens because the breaking of the symmetry allows the

system to become unstable and accumulate mechanical energies in the resonators. Optomechanical nonlinearity comes into play to produce steady mechanical oscillations to generate HOSs. Therefore, our approach enables accurate manipulation of optical spectral lines through the manipulation of the mechanical coupling rate, paving the way for its utilization in a compact, low-power integrated chip-scale device. Furthermore, we presented evidence of synchronization near EP under the condition of weak mechanical resonance frequency differences, in which two optical spectra are generated with similar envelopes. Therefore, the generation of synchronized wideband spectra with equidistant lines based on the EP offers a highly promising platform for various applications, including optical communication technology, optical read-out of mechanical synchronization processes [27], memory applications, and remote clock-timing synchronization [44].

Currently, our system of study can be experimentally realized by using an optical-fiber-based optomechanical cavity or using a nanomechanical beam inside a superconducting transmission-line microwave cavity as mentioned in [25]. The mechanical resonators in the system may be coupled using coupling overhang [45,46]. Since our study relies on the variation of the mechanical coupling rate, this variation can be achieved by utilizing the piezoelectric effect [47], photothermal effect [48], or electrostatic force [49] on the overhang.

#### APPENDIX A: LINEAR STABILITY ANALYSIS

As mentioned in the main text, the nonlinear dynamical equation (2) is linearized to a form given by  $\frac{d\Psi}{dt} = M\Psi$ . The  $8 \times 8$  matrix  $M$  is given as

$$M = \begin{pmatrix} -(i\Delta_1 + \frac{\kappa}{2}) & 0 & 0 & 0 & 0 & 0 & 0 & 0 \\ 0 & -(i\Delta_1 + \frac{\kappa}{2}) & 0 & 0 & 0 & 0 & 0 & 0 \\ 0 & 0 & -(i\Delta_2 + \frac{\kappa}{2}) & 0 & 0 & 0 & 0 & 0 \\ 0 & 0 & 0 & -(i\Delta_2 + \frac{\kappa}{2}) & 0 & 0 & 0 & 0 \\ g_0\bar{a}_1^* & g_0\bar{a}_1 & 0 & 0 & \omega_{m_1} & 0 & 0 & 0 \\ 0 & 0 & 0 & 0 & -\omega_{m_1} & -\frac{\gamma_{m_1}}{2} & J & 0 \\ 0 & 0 & 0 & 0 & 0 & 0 & 0 & \omega_{m_2} \\ 0 & 0 & g_0\bar{a}_2^* & g_0\bar{a}_2 & J & 0 & -\omega_{m_2} & -\frac{\gamma_{m_2}}{2} \end{pmatrix}. \quad (\text{A1})$$

#### APPENDIX B: OTHER POSSIBLE COUPLED-CAVITY CONFIGURATIONS

We may have mechanical gain-gain and loss-loss coupled optomechanical cavities, and to implement the gain-gain (loss-loss) configuration, both cavities are driven by blue-detuned (red-detuned) cw lasers. Through linear stability analysis, we show how these configurations offer less flexibility in controlling sidebands using cw lasers than the gain-loss configuration. From Fig. 10, we see that the mechanical loss-loss configuration does not invoke any finite mechanical oscillations for a large range of coupling rate ( $1 \times 10^{-2}\kappa \leq J \leq$

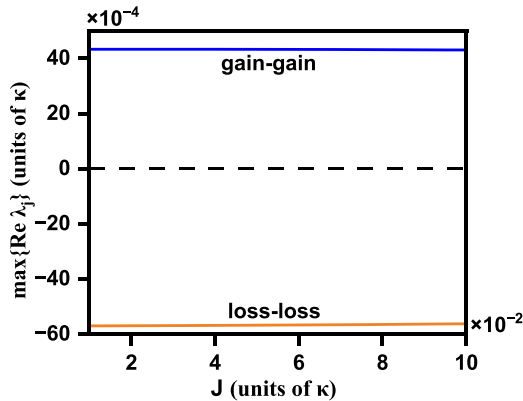


FIG. 10. Stability regions for the case of effective mechanical gain-gain and loss-loss configurations. The parameters are the same as in Sec. III. However, for the gain-gain (loss-loss) configuration we fixed  $\Delta_1 = \Delta_2 = \omega_m$  ( $\Delta_1 = \Delta_2 = -\omega_m$ ).

$10 \times 10^{-2}\kappa$ ) because the system falls in a stable state and, therefore, HOS is absent. On the other hand, the mechanical gain-gain system may have finite oscillations because the system falls in the unstable region. But a transition between the stable and unstable regimes is absent, which would ultimately cause deterministic generation and control of the HOS to fail.

#### APPENDIX C: FREQUENCY SPACING OF THE HOS

We want to analytically verify the amount of frequency spacing for the spectra in Figs. 9(a) and 9(e). Numerically,

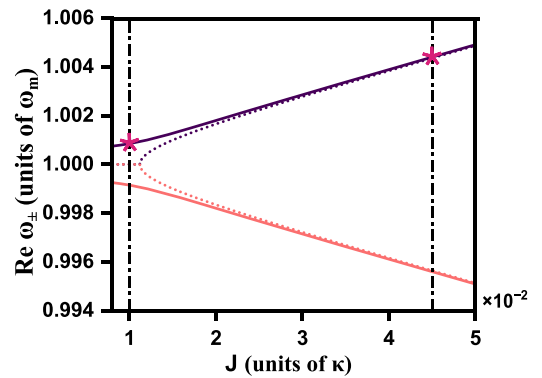


FIG. 11. The dotted lines are for the  $\mathcal{PT}$ -symmetric case when  $\Delta\omega = 0$ . The solid lines show the splitting of  $\text{Re } \omega_+$  (violet) and  $\text{Re } \omega_-$  (orange) for  $\Delta\omega = 1.2 \times 10^{-3}\omega_m$ . The left and right vertical lines correspond to the asynchronous and synchronized spectra at  $J = 1 \times 10^{-2}\kappa$  and  $J = 4.5 \times 10^{-2}\kappa$ , respectively. The stars show the dominance of the upper supermode in deciding the frequency spacing of the HOS.

the spacings in Figs. 9(a) and 9(e) are about  $1.003\omega_m$  and  $1.001\omega_m$ , respectively. The real part of  $\omega_{\pm}$  from Eq. (11) is written in the form

$$\text{Re } \omega_{\pm} = \frac{\omega_{m_1} + \omega_{m_2}}{2} \pm \sqrt{\frac{\eta^2 + \left(\Delta\omega \frac{\gamma_{\text{eff}_1} + \gamma_{\text{eff}_2}}{4}\right)^2}{2} + \eta} \quad (\text{C1})$$

and plotted with varying coupling rate  $J$  for fixed  $\Delta\omega = 1.2 \times 10^{-3}\omega_m$  in Fig. 11. We observe that because of the

finite frequency mismatch, the degeneracy of the supermodes is absent near the EP. The left dash-dotted vertical line is the demonstration point (see the lower yellow dot in Fig. 7) of our asynchronized spectrum, and  $\text{Re } \omega_{+}$  at this line takes the value of  $1.0008\omega_m$ . Similarly,  $\text{Re } \omega_{+}$  at the right dash-dotted vertical line where our synchronized spectrum (upper yellow dot in Fig. 7) is shown takes the value of  $1.004\omega_m$ . So the frequency spacings obtained numerically are similar to the ones obtained analytically. Therefore, once the mechanical resonators acquire limit cycles, the locked frequency will follow the upper mode with eigenfrequency  $\text{Re } \omega_{+}$ , and the frequency spacing in the optical spectrum will be decided based on that.

- 
- [1] M. Aspelmeyer, T. J. Kippenberg, and F. Marquardt, Cavity optomechanics, *Rev. Mod. Phys.* **86**, 1391 (2014).
- [2] H. Rokhsari, T. J. Kippenberg, T. Carmon, and K. J. Vahala, Radiation-pressure-driven micro-mechanical oscillator, *Opt. Express* **13**, 5293 (2005).
- [3] J. B. Khurgin, M. W. Pruessner, T. H. Stievater, and W. S. Rabinovich, Laser-Rate-Equation Description of Optomechanical Oscillators, *Phys. Rev. Lett.* **108**, 223904 (2012).
- [4] H. Rokhsari, T. Kippenberg, T. Carmon, and K. Vahala, Theoretical and experimental study of radiation pressure-induced mechanical oscillations (parametric instability) in optical microcavities, *IEEE J. Sel. Top. Quantum Electron.* **12**, 96 (2006).
- [5] T. Carmon, H. Rokhsari, L. Yang, T. J. Kippenberg, and K. J. Vahala, Temporal Behavior of Radiation-Pressure-Induced Vibrations of an Optical Microcavity Phonon Mode, *Phys. Rev. Lett.* **94**, 223902 (2005).
- [6] M. Poot, K. Y. Fong, M. Bagheri, W. H. P. Pernice, and H. X. Tang, Backaction limits on self-sustained optomechanical oscillations, *Phys. Rev. A* **86**, 053826 (2012).
- [7] M.-A. Miri, G. D'Aguzzo, and A. Alù, Optomechanical frequency combs, *New J. Phys.* **20**, 043013 (2018).
- [8] Y. K. Chembo and N. Yu, Modal expansion approach to optical-frequency-comb generation with monolithic whispering-gallery-mode resonators, *Phys. Rev. A* **82**, 033801 (2010).
- [9] H. Xiong, L.-G. Si, X.-Y. Lü, X. Yang, and Y. Wu, Carrier-envelope phase-dependent effect of high-order sideband generation in ultrafast driven optomechanical system, *Opt. Lett.* **38**, 353 (2013).
- [10] S. Weis, R. Rivière, S. Deléglise, E. Gavartin, O. Arcizet, A. Schliesser, and T. J. Kippenberg, Optomechanically induced transparency, *Science* **330**, 1520 (2010).
- [11] C. Solaro, C. Debavelaere, P. Cladé, and S. Guellati-Khelifa, Atom Interferometer Driven by a Picosecond Frequency Comb, *Phys. Rev. Lett.* **129**, 173204 (2022).
- [12] S. A. Diddams, L. Hollberg, L.-S. Ma, and L. Robertsson, Femtosecond laser-based optical clockwork with instability  $\leq 6.3 \times 10^{-16}$  in 1 s, *Opt. Lett.* **27**, 58 (2002).
- [13] T. Fortier and E. Baumann, 20 years of developments in optical frequency comb technology and applications, *Commun. Phys.* **2**, 153 (2019).
- [14] C. Cao, S.-C. Mi, T.-J. Wang, R. Zhang, and C. Wang, Optical high-order sideband comb generation in a photonic molecule optomechanical system, *IEEE J. Quantum Electron.* **52**, 1 (2016).
- [15] L.-Y. He, Parity-time-symmetry-enhanced sideband generation in an optomechanical system, *Phys. Rev. A* **99**, 033843 (2019).
- [16] H. Jing, S. K. Özdemir, X. Y. Lü, J. Zhang, L. Yang, and F. Nori,  $\mathcal{PT}$ -Symmetric Phonon Laser, *Phys. Rev. Lett.* **113**, 053604 (2014).
- [17] X.-Y. Lü, H. Jing, J.-Y. Ma, and Y. Wu,  $\mathcal{PT}$ -Symmetry-Breaking Chaos in Optomechanics, *Phys. Rev. Lett.* **114**, 253601 (2015).
- [18] W. Li, Y. Jiang, C. Li, and H. Song, Parity-time-symmetry enhanced optomechanically-induced-transparency, *Sci. Rep.* **6**, 31095 (2016).
- [19] P. Djorwe, Y. Pennec, and B. Djafari-Rouhani, Exceptional Point Enhances Sensitivity of Optomechanical Mass Sensors, *Phys. Rev. Appl.* **12**, 024002 (2019).
- [20] Z.-X. Liu, H. Xiong, and Y. Wu, Generation and amplification of a high-order sideband induced by two-level atoms in a hybrid optomechanical system, *Phys. Rev. A* **97**, 013801 (2018).
- [21] P. Djorwe, J. Effa, and S. N. Engo, Multistability, staircases, and optical high-order sideband combs in optomechanics, *J. Opt. Soc. Am. B* **37**, A36 (2020).
- [22] L. Zhang and H.-Y. Kong, Self-sustained oscillation and harmonic generation in optomechanical systems with quadratic couplings, *Phys. Rev. A* **89**, 023847 (2014).
- [23] Y.-P. Gao, X.-C. Liu, K. Wang, and Y. Zhang, Dissipation assisted frequency comb and chaos generation in the optomechanics, *IEEE Photonics J.* **14**, 1 (2021).
- [24] F. Marquardt, J. G. E. Harris, and S. M. Girvin, Dynamical Multistability Induced by Radiation Pressure in High-Finesse Micromechanical Optical Cavities, *Phys. Rev. Lett.* **96**, 103901 (2006).
- [25] X.-W. Xu, Y.-X. Liu, C.-P. Sun, and Y. Li, Mechanical  $\mathcal{PT}$  symmetry in coupled optomechanical systems, *Phys. Rev. A* **92**, 013852 (2015).
- [26] J. Li, Z.-H. Zhou, S. Wan, Y.-L. Zhang, Z. Shen, M. Li, C.-L. Zou, G.-C. Guo, and C.-H. Dong, All-Optical Synchronization of Remote Optomechanical Systems, *Phys. Rev. Lett.* **129**, 063605 (2022).
- [27] J. Sheng, X. Wei, C. Yang, and H. Wu, Self-Organized Synchronization of Phonon Lasers, *Phys. Rev. Lett.* **124**, 053604 (2020).

- [28] C.-G. Liao, R.-X. Chen, H. Xie, M.-Y. He, and X.-M. Lin, Quantum synchronization and correlations of two mechanical resonators in a dissipative optomechanical system, *Phys. Rev. A* **99**, 033818 (2019).
- [29] Y. Hu, S. Ding, Y. Qin, J. Gu, W. Wan, M. Xiao, and X. Jiang, Generation of Optical Frequency Comb via Giant Optomechanical Oscillation, *Phys. Rev. Lett.* **127**, 134301 (2021).
- [30] W. Li, C. Li, and H. Song, Theoretical realization and application of parity-time-symmetric oscillators in a quantum regime, *Phys. Rev. A* **95**, 023827 (2017).
- [31] S. Chakraborty and A. K. Sarma, Delayed sudden death of entanglement at exceptional points, *Phys. Rev. A* **100**, 063846 (2019).
- [32] A. Schliesser, P. Del'Haye, N. Nooshi, K. J. Vahala, and T. J. Kippenberg, Radiation Pressure Cooling of a Micromechanical Oscillator Using Dynamical Backaction, *Phys. Rev. Lett.* **97**, 243905 (2006).
- [33] J. D. Teufel, J. W. Harlow, C. A. Regal, and K. W. Lehnert, Dynamical Backaction of Microwave Fields on a Nanomechanical Oscillator, *Phys. Rev. Lett.* **101**, 197203 (2008).
- [34] C. Genes, D. Vitali, P. Tombesi, S. Gigan, and M. Aspelmeyer, Ground-state cooling of a micromechanical oscillator: Comparing cold damping and cavity-assisted cooling schemes, *Phys. Rev. A* **77**, 033804 (2008).
- [35] Ş. K. Özdemir, S. Rotter, F. Nori, and L. Yang, Parity-time symmetry and exceptional points in photonics, *Nat. Mater.* **18**, 783 (2019).
- [36] C. M. Bender and S. Boettcher, Real Spectra in Non-Hermitian Hamiltonians Having  $\mathcal{PT}$  Symmetry, *Phys. Rev. Lett.* **80**, 5243 (1998).
- [37] H. Xu, D.-G. Lai, Y.-B. Qian, B.-P. Hou, A. Miranowicz, and F. Nori, Optomechanical dynamics in the  $\mathcal{PT}$ - and broken- $\mathcal{PT}$ -symmetric regimes, *Phys. Rev. A* **104**, 053518 (2021).
- [38] J. D. Cohen, S. M. Meenehan, G. S. MacCabe, S. Gröblacher, A. H. Safavi-Naeini, F. Marsili, M. D. Shaw, and O. Painter, Phonon counting and intensity interferometry of a nanomechanical resonator, *Nature (London)* **520**, 522 (2015).
- [39] M. Eichenfield, R. Camacho, J. Chan, K. J. Vahala, and O. Painter, A picogram- and nanometre-scale photonic-crystal optomechanical cavity, *Nature (London)* **459**, 550 (2009).
- [40] P. Djorwe, Y. Pennec, and B. Djafari-Rouhani, Frequency locking and controllable chaos through exceptional points in optomechanics, *Phys. Rev. E* **98**, 032201 (2018).
- [41] E. X. DeJesus and C. Kaufman, Routh-Hurwitz criterion in the examination of eigenvalues of a system of nonlinear ordinary differential equations, *Phys. Rev. A* **35**, 5288 (1987).
- [42] A. A. Clerk, M. H. Devoret, S. M. Girvin, F. Marquardt, and R. J. Schoelkopf, Introduction to quantum noise, measurement, and amplification, *Rev. Mod. Phys.* **82**, 1155 (2010).
- [43] P. Djorwé, Y. Pennec, and B. Djafari-Rouhani, Self-organized synchronization of mechanically coupled resonators based on optomechanics gain-loss balance, *Phys. Rev. B* **102**, 155410 (2020).
- [44] J.-D. Deschênes, L. C. Sinclair, F. R. Giorgetta, W. C. Swann, E. Baumann, H. Bergeron, M. Cermak, I. Coddington, and N. R. Newbury, Synchronization of Distant Optical Clocks at the Femtosecond Level, *Phys. Rev. X* **6**, 021016 (2016).
- [45] S. Márquez, M. Alvarez, J. A. Plaza, L. G. Villanueva, C. Dominguez, and L. M. Lechuga, Asymmetrically coupled resonators for mass sensing, *Appl. Phys. Lett.* **111**, 113101 (2017).
- [46] A. Bhaskar, M. Walth, R. H. Rand, and A. T. Zehnder, Synchronization in pairs of opto-thermally driven mechanically coupled micro-oscillators, *J. Microelectromech. Syst.* **32**, 136 (2022).
- [47] H. Okamoto, A. Gourgout, C.-Y. Chang, K. Onomitsu, I. Mahboob, E. Y. Chang, and H. Yamaguchi, Coherent phonon manipulation in coupled mechanical resonators, *Nat. Phys.* **9**, 480 (2013).
- [48] H. Okamoto, T. Kamada, K. Onomitsu, I. Mahboob, and H. Yamaguchi, Optical tuning of coupled micromechanical resonators, *Appl. Phys. Express* **2**, 062202 (2009).
- [49] P. Huang, P. Wang, J. Zhou, Z. Wang, C. Ju, Z. Wang, Y. Shen, C. Duan, and J. Du, Demonstration of Motion Transduction Based on Parametrically Coupled Mechanical Resonators, *Phys. Rev. Lett.* **110**, 227202 (2013).